Supplemental Document

Label- and slide-free tissue histology using 3D epi-mode quantitative phase imaging and virtual hematoxylin and eosin staining: supplement

Tanishq Mathew Abraham,[1] Paloma Casteleiro Costa,[2] Caroline Filan,[3] Zhe Guang,[4] Zhaobin Zhang,[5,6] Stewart Neill,[5,7] Jeffrey J. Olson,[5,6] Richard Levenson,[8] and Francisco E. Robles[4,*]

[1]*Department of Biomedical Engineering, University of California, Davis, California 95616, USA*
[2]*School of Electrical and Computer Engineering, Georgia Institute of Technology, Atlanta, Georgia 30332, USA*
[3]*George W. Woodruff School of Mechanical Engineering, Georgia Institute of Technology, Atlanta, Georgia 30332, USA*
[4]*Wallace H. Coulter Department of Biomedical Engineering, Georgia Institute of Technology, Atlanta, Georgia 30332, USA*
[5]*Winship Cancer Institute, Emory University, Atlanta, Georgia 30332, USA*
[6]*Department of Neurosurgery, Emory University School of Medicine, Atlanta, Georgia 30332, USA*
[7]*Department of Pathology & Laboratory Medicine, Emory University School of Medicine, Atlanta, Georgia 30332, USA*
[8]*Department of Pathology and Laboratory Medicine, UC Davis Health, Sacramento, California 95817, USA*
[*]*robles@gatech.edu*

Supplement DOI: https://doi.org/10.6084/m9.figshare.24438085

Parent Article DOI: https://doi.org/10.1364/OPTICA.502859

Supplementary Information

Supplementary Note 1: Intensity inversion required for optimal CycleGAN conversion

We found it necessary to invert the grayscale values of the native qOBM images, this is done in order to render the nuclei to appear dark against a lighter background (as they typically appear on H&E). If this step is not taken, the nuclei in qOBM are frequently converted by the CycleGAN into white areas in vH&E (green arrows; **Supp Fig. 1**) while the darker cytoplasmic regions in qOBM are rendered erroneously as nuclei (blue arrows; **Supp Fig. 1**). A similar phenomenon was observed for virtual re-staining of MUSE, another microscopy modality, in Abraham et al.[1]

Supplementary Note 2: Effect of model size on CycleGAN performance

We note that CycleGAN model size is an important property that affects conversion quality. **Supplementary Figure 2** compares the conversions with a small model size/capacity (three layers in the discriminators, nine residual blocks in the generators) and large model size (six layers in the discriminators, twelve residual blocks in the generators) to the conversions of four separate CycleGANs with a small model capacity trained on images of each of the four observed subtypes. These results indicate that the small model size can capture histological features of individual tissue subtypes, but was unable to do so for multiple combined subtypes. Instead, as determined by visual examination, a larger model capacity was necessary to obtain conversions that capture the diversity of histological features seen in the multiple tissue subtypes.

Supplementary Note 3: Additional comments on the performance difference between qOBM-to-vH&E and differential phase contrast (DPC)-to-vH&E

Supplementary Figure 3 illustrates a notable performance advantage in the qOBM-to-H&E conversion compared to the DPC-to-H&E conversion (using 1 DPC image **(C,G)** or the two orthogonal DPC images **(D,H)**). It is important to note that the complexity of the networks used for these conversions is equivalent to the qOBM-to-H&E network, and all have been trained using identical datasets and training epochs. Data preprocessing remains minimal in all scenarios, although additional processing has been applied to the DPC images to enhance illumination balance across the images.

Several factors contribute to the observed difference in vH&E translation performance for both modalities. First, qOBM images exhibit superior detail compared to DPC images, as they contain information from all angles of illumination. Second, the qOBM images are quantitative and possess a more natural appearance than the qualitative phase gradient DPC images. Thus, the qOBM structural characteristics align more closely with those observed in H&E brightfield, making the operations required by the network for the conversion converge faster. It is possible that with significantly more data, the DPC images could provide successful vH&E translations.

Supplementary Note 4: Additional comments on the performance of the classifier developed to differentiate tumors from healthy tissue.

The classifier trained on H&E images from the 9L gliosarcoma tumor model to differentiate tumors from healthy tissue shows excellent accuracy when tested on vH&E images (95.2 ± 2.8%). Nevertheless, it is interesting to note which image types were misclassified. As the confusion matrix of the classifier applied to vH&E images shows (**Fig. 5B**), the misclassified regions are false positives, indicating that the CycleGAN conversion occasionally imparted tumor-like features to healthy images. As shown in

Supplementary Figure 4, the misclassified regions are primarily a result of the CycleGAN hallucinating dark (hyperchromatic) tumor nuclei around blood vessels in otherwise acellular cortex region (**Supp Fig. 4A-B**) and basal ganglia (**Supp Fig. 4C-D**). Similar to the liver results presented above, this suggest that the network at times struggled to interpret structures around blood vessels which had a different appearance in the fresh tissues compared to the processed tissues. Again, it is likely that such failures can be mitigated with improved training of the qOBM-to-vH&E CycleGAN, using larger datasets or alternatively, unpaired image-to-image translation algorithms.

Supplementary Note 5: Generalization of CycleGAN trained on rat to human specimens

To examine the generalization of the qOBM-to-vH&E conversion, we took a neural network trained on rat images and applied it to the qOBM images of human specimens (**Supp Fig. 5A-B**). We observed that nuclear detail remained present, but the CycleGAN had a tendency to render nuclei as red blood cells, inappropriately convert whitespaces, and hallucinate other details (**Supp Fig. 5C-D**). This motivated the use of transfer learning to improve conversion efforts on the human glioma images.

Supplementary Note 6: Field of view considerations

qOBM imaging has been demonstrated with a magnification down to 20x (0.45 NA) which yields a FOV of ~800 μm X 800 μm, and ~ 1 μm lateral resolution, which is enough to enable cellular and subcellular contrast to identify tumor margins [Ref. 20 in main text]. Larger FOVs require lower magnification and (typically) lower NA. While imaging with qOBM is possible at these lower magnifications, the level of cellular detail drops significantly, mostly limited by the 1/(NA)^2 dependance in the depth of field, which gives the axial resolution. In this work, we chose to study the qOBM-to-VH&E translation on images taken with a 60x objective, as they best resemble the structures captured by the handheld probe [44].

To explore larger fields of view, we have imaged a freshly excised mouse brain with a 10x objective (0.25 NA). Results are presented in **Supplementary Fig. 9**. This configuration allows for a field of view of 1.7 mm X 1.7 mm, and a lateral resolution of ~ 1.75 μm, but axial resolution of ~30 μm. As seen in the figure, the contrast provided by this configuration allows for large views of the tissue structure, with significantly more limited cellular contrast.

Supplementary Figures

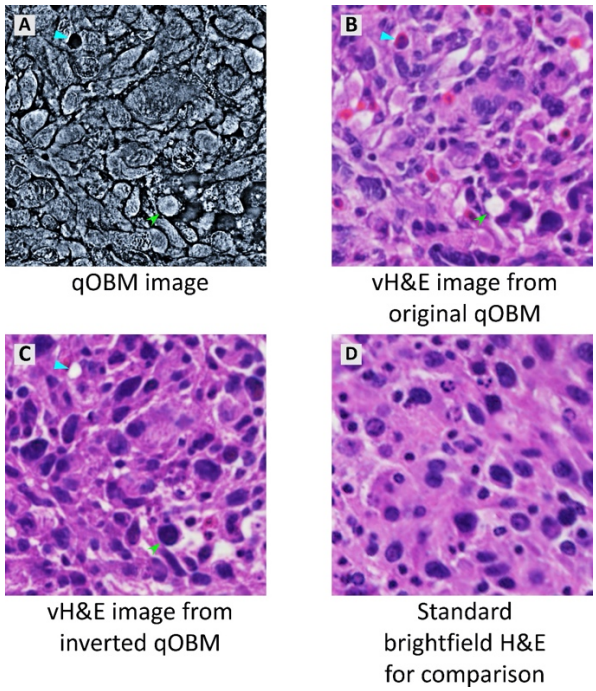

Supplementary Figure 1 - qOBM-to-vH&E conversion with original qOBM images. A Label-free 60x qOBM image of a rat brain tumor region with spherical epithelioid cells. **B** vH&E produced by CycleGAN trained with the original qOBM images of the rat brain tumor regions with spherical epithelioid cells. **C** vH&E produced by CycleGAN trained with the contrast-inverted qOBM images of the rat brain tumor regions with spherical epithelioid cells. **D** Standard brightfield H&E image provided for comparison. Arrows highlight specific examples of inaccuracy during conversion.

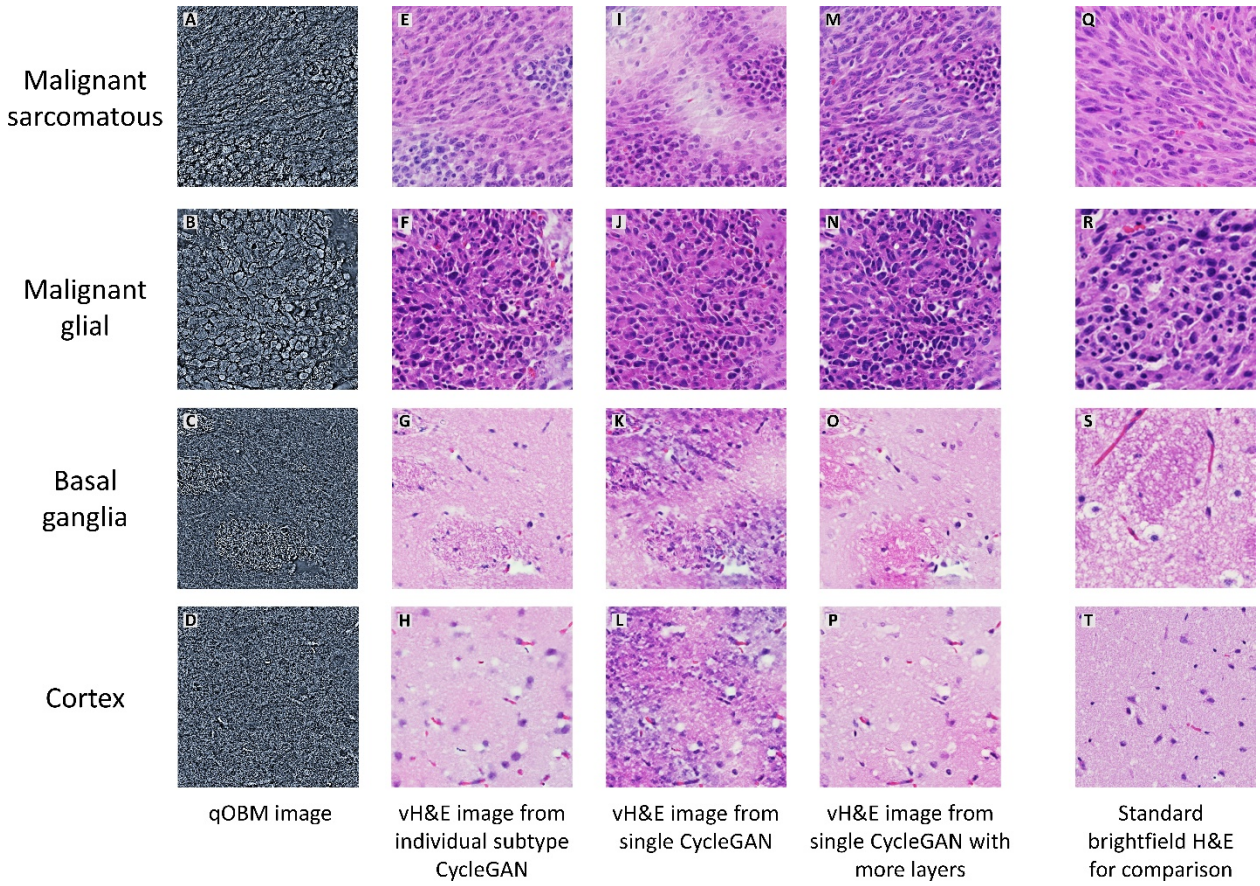

Supplementary Figure 2 - qOBM-to-vH&E conversion on brain tissue subtypes using CycleGANs with different training setups. A-D Label-free 60x qOBM images of each of the four rat brain tissue subtypes. **E-H** Corresponding vH&E images produced by separate CycleGANs for each of the four rat brain tissue subtypes. **I-L** Corresponding vH&E images produced by a single CycleGAN trained on all four rat brain tissue subtypes simultaneously. **M-P** Corresponding vH&E images produced by a single CycleGAN with more layers, trained on all four rat brain tissue subtypes simultaneously. **Q-T** Standard brightfield H&E images of the same tissue subtypes, provided for comparison.

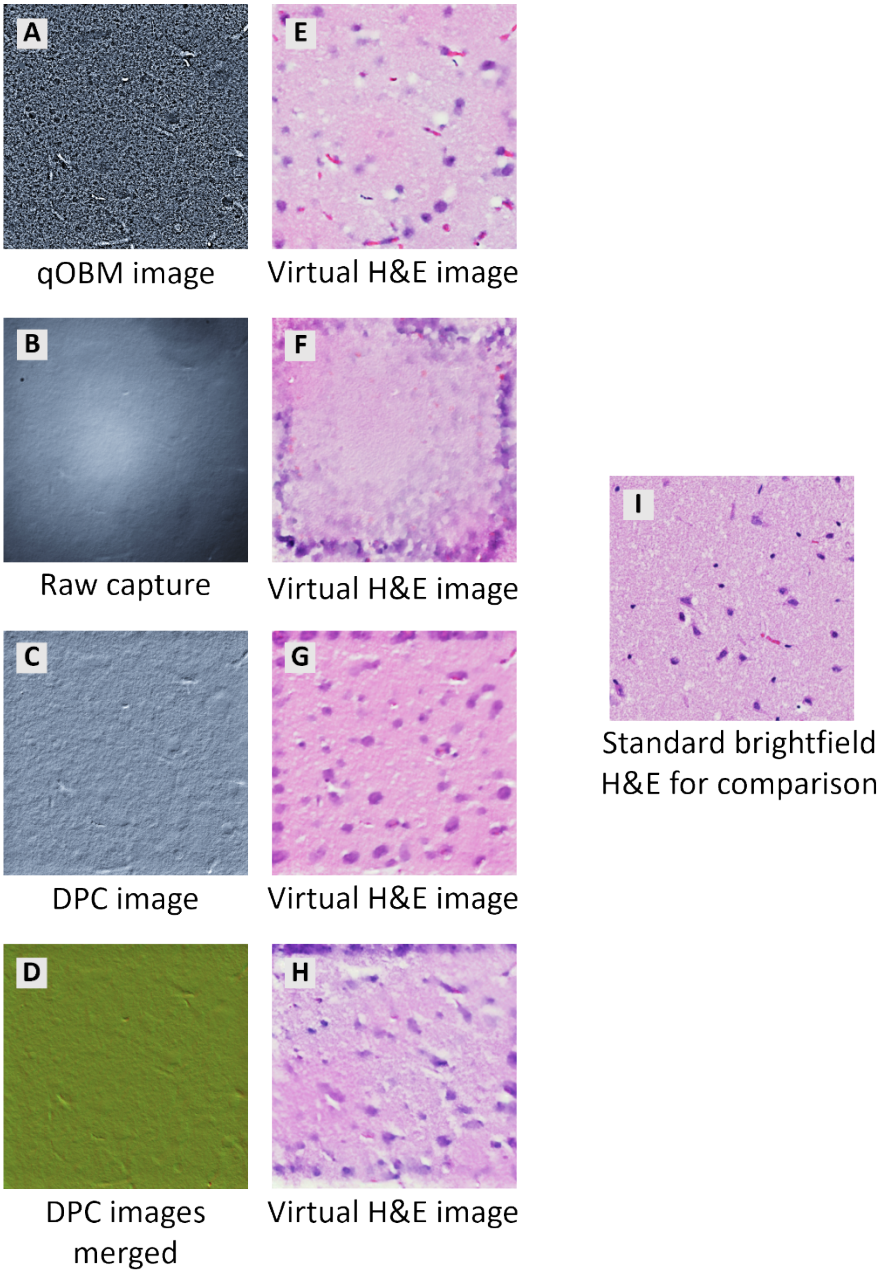

Supplementary Figure 3 - Example vH&E conversions by CycleGANs trained on single capture, DPC, and qOBM images. A qOBM image of rat brain cortex. **B** One of the raw captures from the same field of view used to reconstruct the qOBM image. **C** One of the DPC images from the same field of view used to reconstruct the qOBM image. **D** Pair of orthogonal DPC images from the same field of view encoded in the *Red* and *Green* channels of an RGB image, respectively. The *Blue* channel is left null. **E** vH&E image produced by a CycleGAN trained on rat brain cortex qOBM and H&E images. **F** vH&E image produced by a CycleGAN trained on rat brain cortex single capture and H&E images. **G** vH&E image produced by a CycleGAN trained on rat brain cortex DPC and H&E images. **H** vH&E image produced by a CycleGAN trained on rat brain cortex merged orthogonal DPC images and H&E images. **I** Standard brightfield H&E image provided for comparison.

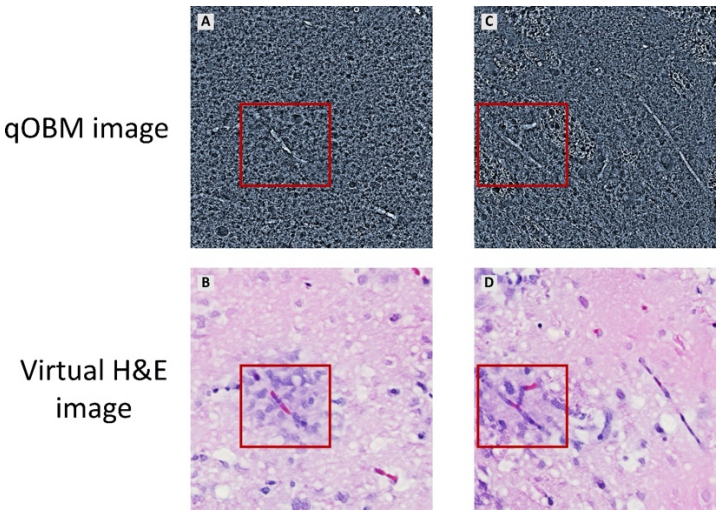

Supplementary Figure 4 - Examples of poor qOBM-to-H&E conversions by the CycleGAN trained on rat brain images. A 60x qOBM image of rat cortex. **B** Corresponding vH&E image. **C** 60x qOBM image from rat basal ganglia. **D** Corresponding vH&E image. Red boxes highlight location of significant conversion error. Conversion errors are primarily observed around vessels which are structures that deviate between the qOBM images of fresh tissues and H&E images of processed tissue sections. In qOBM images of fresh tissues, capillaries are better preserved and continuous; in comparison, capillaries appear fragmented in H&E images of processed tissue sections.

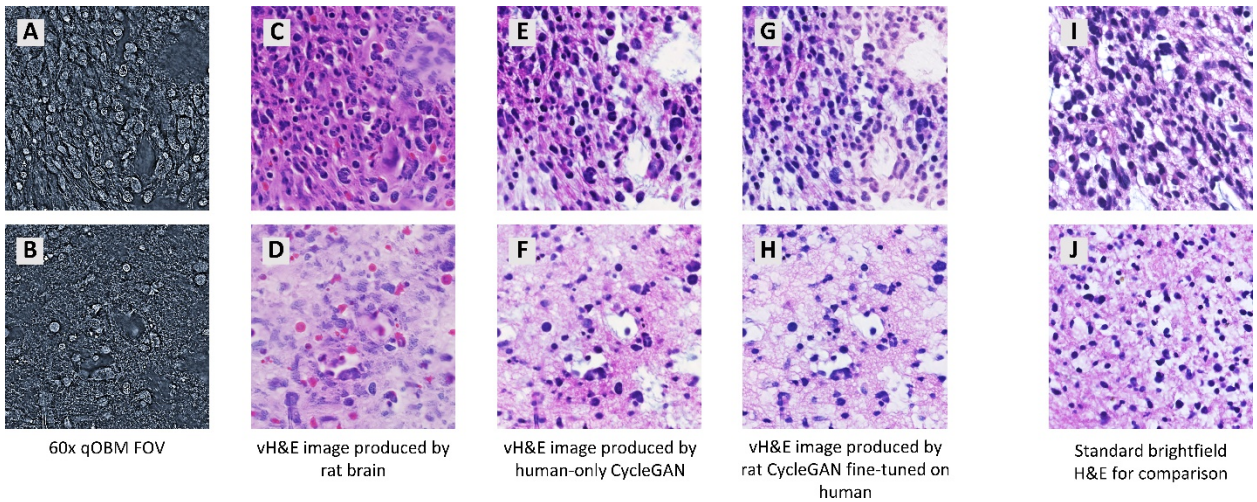

Supplementary Figure 5 - qOBM-to-vH&E conversion of human glioma specimens using CycleGANs with different training and dataset setups. **A-B** Label-free 60x qOBM images of human glioma specimens. **C-D** Corresponding vH&E images produced by the CycleGAN trained on only rat brain images. **E-F** Corresponding vH&E images produced by a CycleGAN trained only on human glioma images. **G-H** Corresponding vH&E images produced by a CycleGAN originally trained on rat brain images and further fine-tuned on human glioma images. This CycleGAN neural network was used for the results presented the main text. **K-L** Standard brightfield H&E images of the same tissue subtypes, provided for comparison.

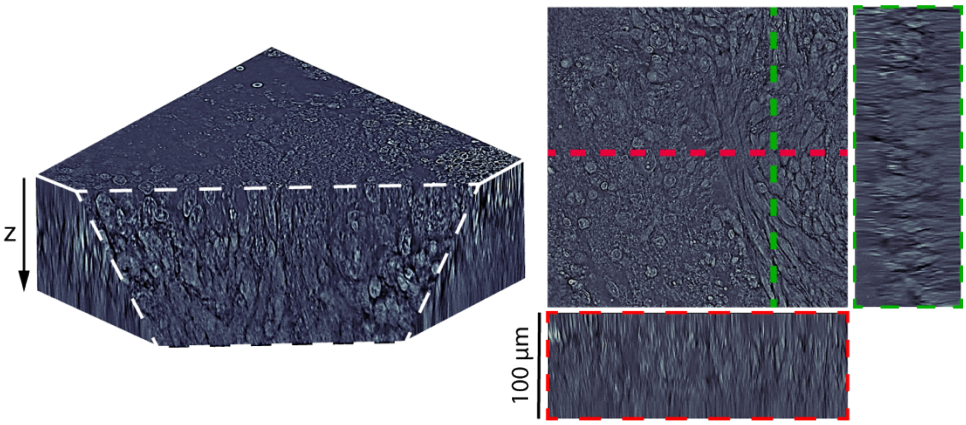

Supplementary Figure 6. qOBM volume, with X-Y, X-Z, and Y-Z cross sections of the volumetric tissue stack displayed in the main text figure 7B.

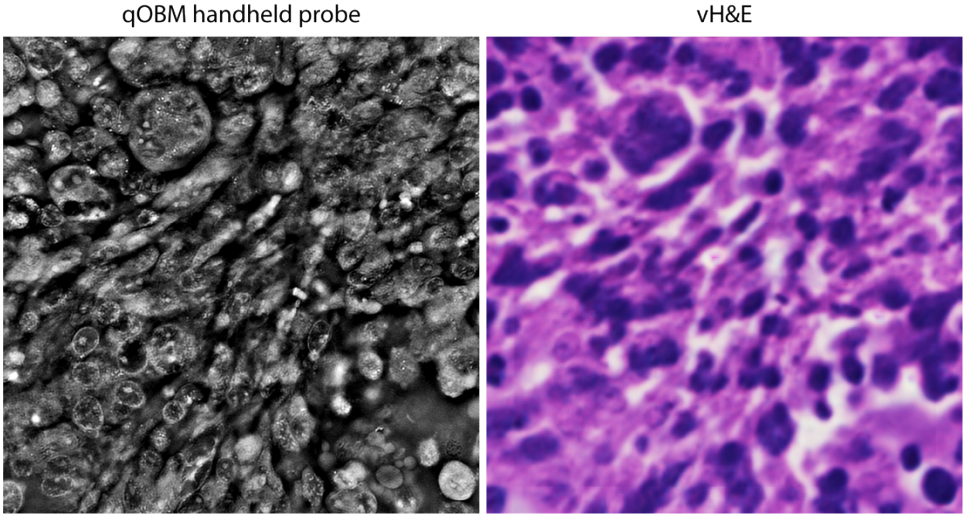

Supplementary Figure 7. qOBM-to-vH&E conversion of mouse brain tumor images with the qOBM hand-held probe . A. qOBM image of freshly excised GL 261 mouse brain tumor tissue. **B.** Corresponding vH&E image using the combined rat qOBM-to-vH&E model. Additional fine-tune the model, which was not trained on this species or tumor type, could substantially improve conversion, but these results are compelling.

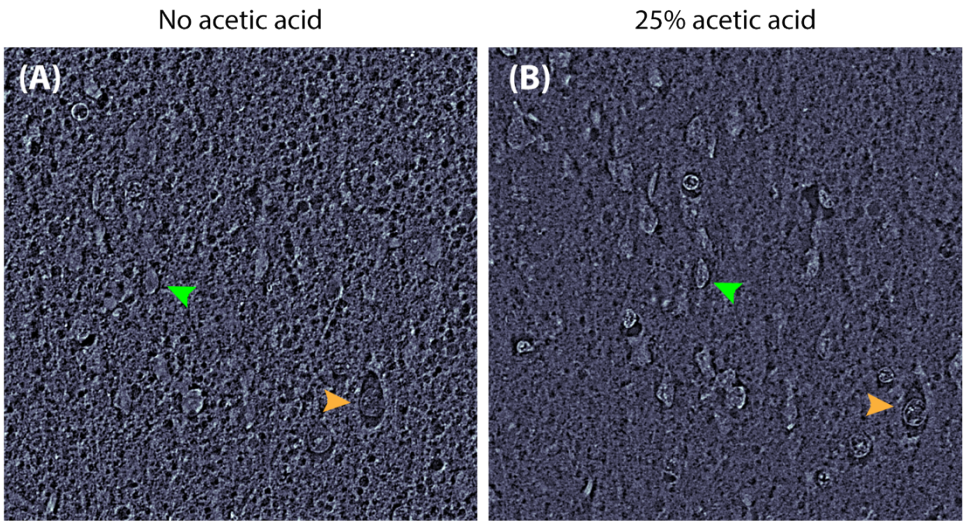

Supplementary Figure 8. Effects of acetic acid staining on qOBM images of fresh brain tissue. A. qOBM image of fresh brain mouse tissue. **B.** qOBM image of the same tissue 30 minutes after being stained with 25% acetic acid. The green and orange arrows indicate the same structures in both images. Although the images are of nearly the same regions, pixel-matched data was not successfully obtained due to significant tissue distortions after AA staining of the soft brain tissue.

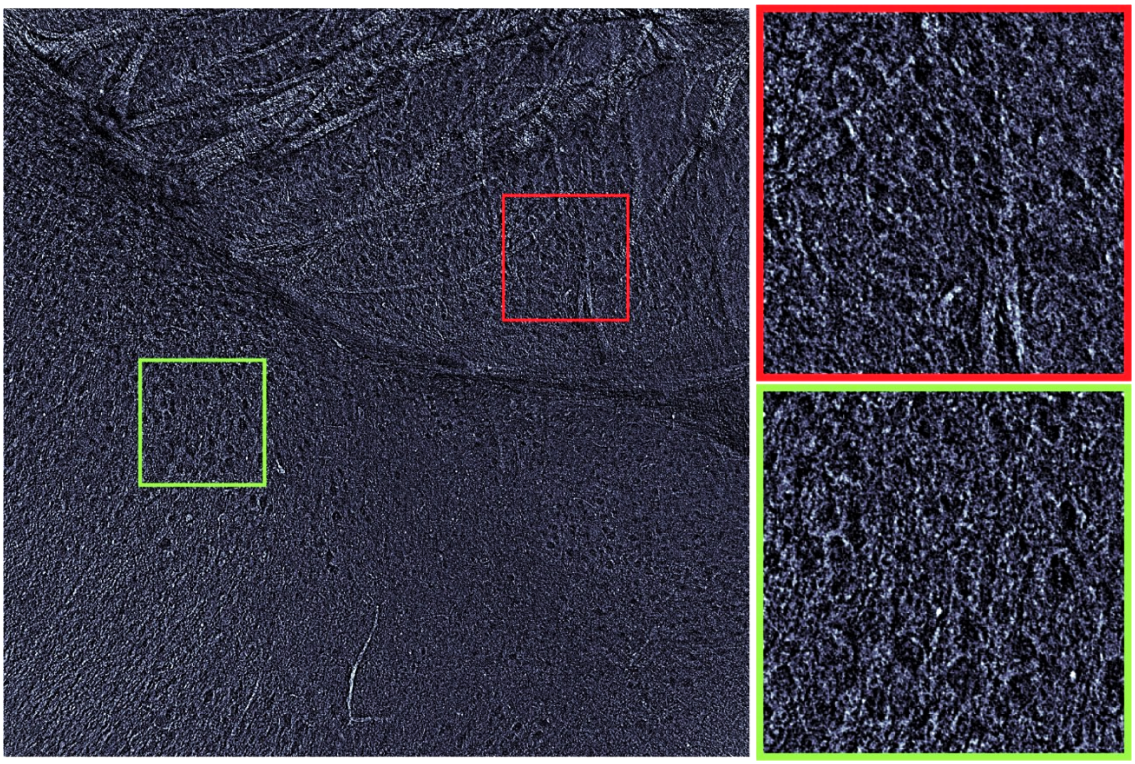

Supplementary Figure 9. qOBM iamge of a freshly excised mouse brain using low magnification (10X) and large field of view. Field of view is 1.7 mm X 1.7 mm, lateral resolution is ~ 1.75 µm but axial resolution of ~30 µm. As seen in the images, the contrast provided by this configuration allows for large views of the tissue structure, with significantly more limited cellular contrast.

Supplementary Table 1

Detailed costs of add-on module to convert brightfield microscope to qOBM		
Item	Quantity	Cost/unit
Arduino Nano Every	1	$13
LuxeonStar Far Red Rebel LED	4	$9.41
LuxeonStar High Alpha Heat Sink	4	$6.30
LuxeonStar BuckPuck DC Driver	4	$10.99
Thorlabs Aspheric Condenser Lens, Ø1", f=16 mm, NA=0.79	8	$20.16
Thorlabs 0.50 NA Step-Index Multimode Fibers (1 meter)	4	$27.95
Thorlabs SMA905 Multimode Connector	4	$12.22
	TOTAL	$441.76
Key components of brightfield microscope in this study		
PCO.edge 4.2 LT (camera in this study)	1	$11,000
Basler monochrome acA1920-150um (alternative camera also used in handheld system)	1	$650
Nikon Plan Fluor ELWD, 60x, 0.7 NA	1	$4,500

Supplementary Videos

Supplementary Video 1 - A depth sweep-through of qOBM images in a volumetric image stack (270 µm x 270 µm x 100 µm) of rat gliosarcoma tissue.

Supplementary Video 2 - A depth sweep-through of vH&E images corresponding to the qOBM images in **Supplementary Video 1**.

Supplementary Video 3 - A depth sweep-through of qOBM images in a volumetric image stack (270 µm x 270 µm x 85 µm) of a freshly excised grade 3 human astrocytoma tissue specimen.

Supplementary Video 4 - A depth sweep-through of vH&E images corresponding to the qOBM images in **Supplementary Video 3**.

Supplementary References

1. Abraham, T., Shaw, A., O'Connor, D., Todd, A. & Levenson, R. Slide-free MUSE Microscopy to H&E Histology Modality Conversion via Unpaired Image-to-Image Translation GAN Models. *ArXiv200808579 Cs Eess* (2020).